



The Society shall not be responsible for statements or opinions advanced in papers or discussion at meetings of the Society or of its Divisions or Sections, or printed in its publications. Discussion is printed only if the paper is published in an ASME Journal. Authorization to photocopy for internal or personal use is granted to libraries and other users registered with the Copyright Clearance Center (CCC) provided \$3/article or \$4/page is paid to CCC, 222 Rosewood Dr., Danvers, MA 01923. Requests for special permission or bulk reproduction should be addressed to the ASME Technical Publishing Department.

Copyright © 1998 by ASME

All Rights Reserved

Printed in U.S.A.

PERFORMANCE OF TURBULENCE MODELS AND NEAR-WALL TREATMENTS IN DISCRETE JET FILM COOLING SIMULATIONS

Jeffrey D. Ferguson, Dibbon K. Walters, and James H. Leylek

Department of Mechanical Engineering

Clemson University

Clemson, SC 29634



BREAK

ABSTRACT

For the first time in the open literature, code validation quality data and a well-tested, highly reliable computational methodology are employed to isolate the true performance of seven turbulence treatments in discrete jet film cooling. The present research examines both computational and high quality experimental data for two length-to-diameter ratios of a row of streamwise injected, cylindrical film holes. These two cases are used to document the performance of the following turbulence treatments: 1) standard k- ϵ model with generalized wall functions; 2) standard k- ϵ model with non-equilibrium wall functions; 3) Renormalization Group k- ϵ (RNG) model with generalized wall functions; 4) RNG model with non-equilibrium wall functions; 5) standard k- ϵ model with two-layer turbulence wall treatment; 6) Reynolds Stress Model (RSM) with generalized wall functions; and 7) RSM with non-equilibrium wall functions. Overall, the standard k- ϵ turbulence model with the two-layer near-wall treatment, which resolves the viscous sublayer, produces results that are more consistent with experimental data.

NOMENCLATURE

A	Van Driest constant = 26	NE	non-equilibrium wall functions
c _p	specific heat at constant pressure [kJ/kg-K]	p	local pressure [N/m ²]
D	diameter of film-hole [m]	P	lateral distance for pitch between adjacent film holes
DR	density ratio = (ρ_f/ρ_∞)	P/D	pitch-to-diameter ratio of film hole
E	constant for wall functions = 9.793	Pr	Prandtl number
h	heat transfer coefficient [W/m ² K]	Pr _t	turbulent Prandtl number
k	turbulent kinetic energy [m ² /s ²]	\dot{q}''	wall heat flux [W/m ²]
KE	standard k- ϵ turbulence model	REF1	streamwise injected cylindrical-hole reference: 1 st case
l	length scale [m]	REF2	streamwise injected cylindrical-hole reference: 2 nd case
L	length of film hole [m]	RNG	Renormalization Group k- ϵ turbulence model
LE	leading edge of coolant jet exit plane	RSM	Reynolds Stress Model
L/D	length-to-diameter ratio of film hole	Re _{fh}	Reynolds number in film-hole based on hole diameter
M	mass flux (or blowing) ratio = (ρV)/(ρU_∞)	Re _x	Reynolds number based on streamwise direction
		Rey	Turbulent Reynolds number (Section 4.4.3)
		T	local fluid temperature [K]
		T*	nondimensional temperature (Section 4.4.1)
		TE	trailing edge of coolant jet exit plane
		TL	turbulence level (%) = (100*(2/3*k) ^{0.5})/U _{&infty}
		u,v,w	velocity component in the x,y,z direction [m/s]
		U	mean velocity [m/s]
		U*	nondimensional velocity (Section 4.4.1)
		V	local velocity vector [m/s]
		V	magnitude of local velocity vector = V [m/s]
		VR	velocity ratio = (V _f /U _{&infty})
		WF	generalized wall functions
		x,y,z	Cartesian coordinate system axes
		y*	alternate nondimensional wall distance (Section 4.4.1)
		α	injection angle measured from the x-z plane [°]
		δ	boundary layer thickness [m]
		ϵ	dissipation rate of turbulent kinetic energy [m ² /s ³]
		κ	von Karman's constant = 0.42
		η	adiabatic effectiveness = (T _{&infty} -T _{aw})/(T _{&infty} -T _j)

$\bar{\eta}$	laterally averaged adiabatic effectiveness
ρ	density [kg/m^3]
τ	shear stress [N/m^3]
μ	dynamic viscosity [$\text{kg}/\text{m}\cdot\text{s}$]
μ_{eff}	effective viscosity [$\text{kg}/\text{m}\cdot\text{s}$]
μ_t	turbulent viscosity [$\text{kg}/\text{m}\cdot\text{s}$]
ν	kinematic viscosity [m^2/s]
ν_T	turbulent kinematic viscosity [m^2/s]

Subscripts

∞	mainstream conditions at crossflow inlet plane
f	with film cooling
j	coolant jet conditions
o	without film cooling
P	condition at point P in the domain
aw	adiabatic wall
w	condition at wall

1. INTRODUCTION

As competition in the global gas turbine marketplace grows more intense, designers require a means of increasing productivity while decreasing capital cost and design cycle time to market new engines. The highly empirical nature of current film-cooling design methodology has created the need for more advanced, physics-based design practices. Tools such as computational fluid dynamics (CFD) and supercomputers have helped usher in a new era of research and rapid prototyping. However, only when CFD is properly verified and applied does it prove to be a useful predictive tool. One of the critical areas of CFD needing understanding and verification is turbulence treatment. In order to isolate and study the true performance of turbulence treatments, great care must be given to the other important aspects of computational simulations, such as proper modeling of flow physics, applying a complete and realistic set of boundary conditions, using a higher order discretization scheme to reduce numerical viscosity, and adequately addressing grid independence and convergence. For the first time in the open literature, this paper isolates and analyzes the true performance of seven turbulence model and near wall treatment combinations in discrete jet film cooling by using a well-tested, highly reliable computational methodology in conjunction with code-validation quality data.

2. LITERATURE REVIEW

2.1 Experimental Studies

The open literature contains a considerable number of studies pertaining to streamwise injected, cylindrical film-cooling jets. Both Pietrzyk et al. (1989) and Sinha et al. (1990) used geometries with L/D parameters representative of those in gas turbines to thoroughly investigate the flow field and the surface cooling effectiveness, respectively. Sen (1995) also used realistic geometries and flow conditions to examine their effects on heat transfer. However, in all cases, the authors needed to use the available data to hypothesize to some degree on the physics governing the results, especially those within the film hole. These particular experimental studies are highlighted because they provide the reference data for the turbulence treatment performance assessment described in the present study.

2.2 Computational Studies

With the rapid development of computer hardware and CFD solver technology, many of the issues that once plagued CFD have been addressed. For example, Demuren (1982) demonstrated the superiority of higher order discretization schemes over first order schemes in reducing numerical viscosity. However, a new set of difficulties has arisen to challenge the effectiveness of CFD. Issues regarding the accuracy of the computational model, boundary conditions, and assumptions of the flow characteristics have proven to be of great importance. For instance, Leylek and Zerkle (1994) showed that the complex flow within the film hole has drastic effects on the flow characteristics downstream of the hole exit. The importance of the three-way coupling of the flow in the plenum, film hole, and crossflow was supported by Garg and Gaugler (1995) in a paper in which they showed significant changes in the surface results with slight changes in jet exit profiles imposed as boundary conditions. Nevertheless, many studies still apply unrealistic boundary conditions. For example, in an analysis of turbulence model performance in confined swirling flows, Sharif and Wong (1994) specified the velocity outlet conditions even though it is impossible to know with certainty these exit conditions *a priori*.

Not only are the simulation model and boundary conditions important, but grid quality and resolution also plays a large role, specifically the issue of grid independence. Grid independence implies that further significant refinements of the grid produce negligible change in the results. Solution-based adaption techniques aid in the process of reaching a grid independent solution by allowing grid nodes to be efficiently concentrated in critical, high gradient regions of the flow field. However, grid independence is not adequately addressed in many papers, specifically those that compare turbulence treatments. Hosseinalipour and Mujumdar (1995) investigate the performance of turbulence models in impinging jet flows using a single block, structured grid. This topology is difficult to bring to grid independence economically since adaption only in specific regions is not possible. Consequently, the authors do not address grid independence.

One of the major difficulties with CFD is prescribing an appropriate turbulence treatment. Although the "perfect" turbulence model has not yet been invented, CFD practitioners must make sensible use of the current models and near-wall treatments, each of which have various strengths and weaknesses. Unfortunately, none of the studies on turbulence treatments for film-cooling problems have yet attempted to address the accuracy of the computational model, boundary conditions, assumptions of the flow characteristics, and grid independence in such a way as to isolate the true performance of these treatments. For instance, Sarkar and Bose (1995) investigate the relative performance of turbulence models in film-cooling applications; however, the authors used an arbitrary jet exit condition that does not adequately model the jet/crossflow interaction in film cooling. In a study of film cooling on airfoils, Garg and Ameri (1997) also use an arbitrary film-hole exit condition and do not address the issue of grid independence.

A computational methodology developed and validated in Walters and Leylek (1997a) emphasized the importance of four issues when consistently accurate predictions are desired:

- proper modeling of the flow physics
- accurate geometry resolution and high quality grid generation

- higher-order discretization scheme
- appropriate turbulence closure model selection

The present study employs the computational methodology outlined in Walters and Leylek (1997a) in such a way that all the known sources of numerical errors are reduced to negligible levels in order to isolate the true behavior of the turbulence treatments.

2.3 Outstanding Issues

Presently, not a single study in the open literature has addressed the critical aspects of a simulation in order to isolate the true performance of turbulence treatments in film-cooling applications. The outstanding issues of these studies can be summarized in this short list:

- Lack of appreciation for the importance of using L/D parameters representative of those used in actual gas turbines
- Lack of three-way coupling of the flow in the coolant supply plenum, film-hole, and crossflow regions
- Use of inexact geometry and coarse or poor quality mesh which do not provide grid independent solutions
- Application of unrealistic boundary conditions to model jet and crossflow interactions
- Use of low order discretization schemes that produce high levels of numerical viscosity

3. PRESENT CONTRIBUTIONS

The present study attempts to isolate and analyze the true performance of several turbulence models and near wall treatments in discrete jet film cooling by the combined use of both code-validation quality data and a well-tested, highly reliable computational methodology. In addition, for the first time in the open literature, the Reynolds Stress Model (RSM) will be compared to the standard two-equation models in film-cooling situations. The turbulence models and near wall treatments to be investigated are as follows:

1. standard k- ϵ model with generalized wall functions
2. standard k- ϵ model with non-equilibrium wall functions
3. RNG model with generalized wall functions
4. RNG model with non-equilibrium wall functions
5. standard k- ϵ model with two-layer zonal wall treatment
6. RSM with generalized wall functions
7. RSM with non-equilibrium wall functions

4. SIMULATION DETAILS

4.1 Methodology

In order to arrive at a solution to the time-averaged, steady Navier-Stokes equations, a multi-block, unstructured/adaptive, pressure-correction code with multi-grid and underrelaxation convergence accelerators was employed. The turbulence models and near wall treatments used are available in Fluent/UNS from Fluent, Inc. as documented in Fluent/UNS (1996). The computational domain and background grid were created using the I-DEAS Solid Modeling and Finite Element Analysis software from SDRC, Inc. After finding a solution using a relatively coarse background grid, the grid was adapted, or refined, in the regions of high gradients in the flow field. The hanging node adaption technique was used in order to preserve the high quality of the background grid. A new converged solution was obtained on the refined grid, and this refinement pro-

cess was repeated until the solution was grid independent. For the wall function cases, the grid independent solution typically contained around 300,000 finite volumes, while the two-layer model used approximately 400,000 finite volumes. Convergence of a solution was established by extremely strict criteria: 1) a drop in all residuals to 0.01% of the relevant inlet fluxes; 2) global mass and energy imbalances of less than 0.01%; 3) less than 0.01% change in the general flow field and pertinent surface parameters, such as adiabatic effectiveness and heat transfer coefficient, upon further iterations; and 4) no change in velocity, total pressure, temperature, k, and ϵ profiles at selected stations. Grid independence was established when further refinement produced changes less than 0.01% in velocity, total pressure, temperature, k, and ϵ profiles at strategic stations in the flow field. This process was duplicated for every case-turbulence model combination. The simulations were run on a Sun HPC 6000 computer with 16 cpu's and 4 GB of RAM. The results were post-processed on an SGI Indigo2 workstation with an R10000 cpu and the IMPACT graphics system. The methodology used in the present study is fully outlined in Walters and Leylek (1997).

4.2 Computational Models and Boundary Conditions

For the present study, the simulations were exact replicas of the experimental studies of Sinha et al. (1990) and Sen (1995). Following the computational model advocated by Leylek and Zerkle (1994), the plenum, film-hole, and crossflow regions for each case were included in the solution domain. Boundary conditions were carefully applied to the crossflow and plenum inlets of each simulation to precisely match the blowing ratio, density ratio, and film-hole Reynolds number of the corresponding experimental study. Each computational domain encompasses one-half of the pitch and uses symmetry planes to model a row of holes.

4.2.1 REF1 Case

The REF1 case was modeled after the experimental study of Sinha et al. (1990). The authors documented only adiabatic effectiveness measurements for a row of streamwise injected, cylindrical film holes. The parameters for the tests of interest in the present study were D=12.7 mm, L/D=1.75, P/D=3, $\alpha=35^\circ$, M=1, and DR=2. The experimental domain extended 19D upstream of the film hole where the wind tunnel boundary layer was suctioned off to allow the formation of a new boundary layer over the test surface. Coolant was injected from a supply plenum beneath the test section. The density ratio was controlled by managing the temperature of the coolant while maintaining the crossflow temperature at 302 K.

The present computational simulation exactly matches the geometry and flow conditions used in the experiments. The origin of the coordinate system is at the downstream-most edge, or trailing edge, of the film hole. In the vertical direction, the computational model extends 10D from the test surface which is far enough from the near field to impose a "slip" condition with zero normal gradients for all dependent variables. For the cases involving wall functions, the domain extends 19D upstream of the leading edge and has a uniform inlet velocity of 20 m/s and inlet temperature of 302 K. The outlet is 30D downstream of the film-hole trailing edge where a constant pressure condition is imposed with all other variables upwinded. The plenum inlet velocity and temperature conditions were applied to insure the correct blowing ratio and density ratio conditions were met. At both the crossflow and plenum inlet planes, turbulence intensity

was 2% and the length scale was 1/10 of the respective inlet extents. All walls were adiabatic.

The domain for the case involving the two-layer near-wall treatment was reduced in order to save computational resources. The inlet extends 8D upstream of the leading edge of the film hole where a boundary layer profile was applied to match the experiments. The outlet is 16D downstream of the trailing edge of the film hole. All other aspects of the simulation matched the cases that used wall functions.

4.2.2 REF2 Case

The REF2 case was modeled after the experimental study of Sen (1995). The authors documented heat transfer measurements for a row of film holes. In the present study, the parameters of interest for the streamwise injected cylindrical film holes are as follows: $L/D=4.0$, $P/D=3$, $\alpha=35^\circ$, $M=1$, $DR=1$, and $Re_m=7000$. At the leading edge of the film hole, the crossflow boundary layer is fully turbulent with $\delta/D \approx 2.1$. The experimental study had a free stream velocity of 10 m/s. The parameters in the present computational study exactly match the flow conditions and geometry of the experimental study. The origin of the coordinate system is at the trailing edge of the film hole. Figure 1 shows a schematic of the overall

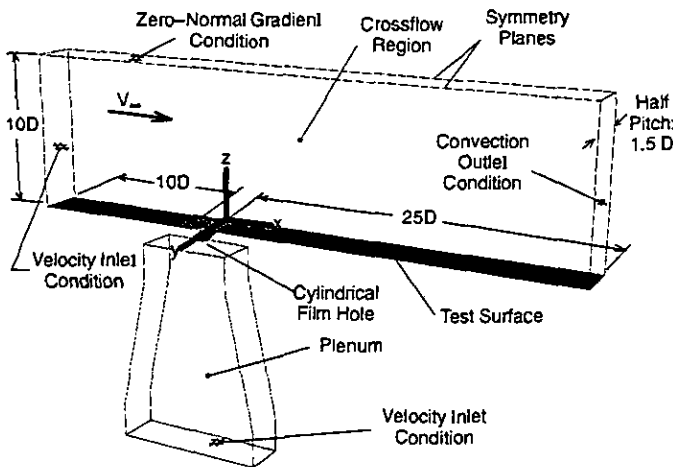


Figure 1. Schematic of computational model of the REF2 case utilized in the present study, showing the plenum, film hole, and crossflow regions with the domain extents and boundary conditions.

extent of the computational domain. In the vertical direction, the domain extends 10D from the test surface where a "slip" condition with zero normal gradients was applied. The inlet plane is placed 10D upstream of the leading edge of the row of film holes where experimental data on the boundary layer and free stream velocity were used to create an inlet profile of all relevant dependent variables. The inlet values for k and ϵ were the same as in the REF1 case. The domain extends 25D downstream of the trailing edge of the film hole to a constant pressure outlet condition with all other dependent variables upwinded. A constant heat flux of 4000 W/m^2 was applied to the test surface. All other walls were adiabatic.

4.3 Turbulence Treatments and Nomenclature

The present study investigates the performance of seven different turbulence treatments. Three different turbulence modeling techniques are used in combination with three different near-wall treatments. Table 1 lists the permutations of these combinations and gives the name of each

case. Sections 4.4 and 4.5 describe each turbulence model and near-wall treatment in more detail.

Table 1: Turbulence Model/Near-wall Treatment Combinations

REF1 Case		
Model	Near-wall Treatment	Case Name
standard k- ϵ	generalized wall functions	REF1-KE-WF
standard k- ϵ	non-equilibrium wall functions	REF1-KE-NE
standard k- ϵ	two-layer	REF1-KE-2L
RNG k- ϵ	generalized wall functions	REF1-RNG-WF
RNG k- ϵ	non-equilibrium wall functions	REF1-RNG-NE
RSM	generalized wall functions	REF1-RSM-WF
RSM	non-equilibrium wall functions	REF1-RSM-NE

REF2 Case		
Model	Near Wall Treatment	Case Name
standard k- ϵ	generalized wall functions	REF2-KE-WF
RNG k- ϵ	generalized wall functions	REF2-RNG-WF
RSM	generalized wall functions	REF2-RSM-WF

In order to maintain consistency throughout the present paper, the following terminology will be employed. "Turbulence model" will refer to the set of equations that yield the actual turbulence quantities: the standard k- ϵ model, the RNG k- ϵ model, and the Reynolds Stress Model (RSM). "Near-wall treatment" will refer to the set of equations used to model turbulence near a solid boundary: generalized wall functions, non-equilibrium wall functions, and the two-layer zonal model. "Turbulence treatment" will refer to the combination of a particular turbulence model and a near wall treatment. Each turbulence treatment is designated by a three-part nomenclature. The first part designates the test case, the second indicates the turbulence model, and the third part identifies the near-wall treatment. For example, REF1-KE-WF refers to the simulations using the REF1 case, the standard k- ϵ turbulence model, and generalized wall functions.

4.4 Turbulence Models

Three different turbulence models were investigated using the REF1 and REF2 cases. Buoyancy terms were neglected for all turbulence models.

4.4.1 Standard k- ϵ Model

The standard k- ϵ turbulence model (Lauder and Spalding, 1972) is a semi-empirical model derived from the Reynolds-averaged Navier-Stokes equations that is valid only for fully turbulent flows. It is based on the Boussinesq hypothesis,

$$-\rho \overline{u_i' u_j'} = \mu_t \left(\frac{\partial u_i}{\partial x_j} + \frac{\partial u_j}{\partial x_i} \right) - \frac{2}{3} \left(\rho k + \mu_t \frac{\partial u_m}{\partial x_m} \right) \delta_{ij} \quad (1)$$

where the turbulent, or eddy, viscosity, μ_t , is defined using the turbulent kinetic energy, k , and its dissipation rate, ϵ , as follows:

$$\mu_t = C_\mu \rho \frac{k^2}{\epsilon} \quad (2)$$

The transport equations for k and ϵ , respectively, are given by:

$$\frac{\partial}{\partial t}(\rho k) + \frac{\partial}{\partial x_i}(\rho u_i k) = \frac{\partial}{\partial x_i} \left[\left(\mu + \frac{\mu_i}{\sigma_k} \right) \frac{\partial k}{\partial x_i} \right] + G_k - \rho \epsilon \quad (3)$$

$$\begin{aligned} \frac{\partial}{\partial t}(\rho \epsilon) + \frac{\partial}{\partial x_i}(\rho u_i \epsilon) &= \frac{\partial}{\partial x_i} \left[\left(\mu + \frac{\mu_i}{\sigma_\epsilon} \right) \frac{\partial \epsilon}{\partial x_i} \right] \\ &+ C_{1\epsilon} \frac{\epsilon}{k} G_k - C_{2\epsilon} \rho \frac{\epsilon^2}{k} \end{aligned} \quad (4)$$

where G_k is the generation of k :

$$G_k = - \rho \overline{u_i' u_j'} \frac{\partial u_j}{\partial x_i} \quad (5)$$

The constants for the $k-\epsilon$ turbulence model are listed in Table 2.

Table 2: Constants for the $k-\epsilon$ Turbulence Model

C_μ	0.09
σ_k	1.0
σ_ϵ	1.3
$C_{1\epsilon}$	1.44
$C_{2\epsilon}$	1.92

4.3.2 RNG $k-\epsilon$ Model

The Renormalization Group (RNG) $k-\epsilon$ turbulence model (Yakhot and Orszag, 1986) is derived from the instantaneous Navier-Stokes equations without employing the Reynolds-averaging technique used in the standard $k-\epsilon$ model. Using Renormalization techniques, it computes an effective viscosity that statistically accounts for the influence of the turbulent motion on the mean flow.

$$\mu_{eff} = \mu \left[1 + \sqrt{\frac{C_\mu}{\mu}} \frac{k}{\sqrt{\epsilon}} \right]^2 \quad (6)$$

Using this effective viscosity, the Navier-Stokes equations can be rewritten in terms of the mean flow quantities only.

$$\frac{\partial}{\partial t}(\rho u_i) + \frac{\partial}{\partial x_j}(\rho u_i u_j) = \frac{\partial}{\partial x_j} \left[\mu_{eff} \left(\frac{\partial u_i}{\partial x_j} + \frac{\partial u_j}{\partial x_i} \right) \right] - \frac{\partial p}{\partial x_i} \quad (7)$$

The following transport equations are used to calculate k and ϵ .

$$\frac{\partial}{\partial t}(\rho k) + \frac{\partial}{\partial x_i}(\rho u_i k) = \frac{\partial}{\partial x_i} \left(\alpha_k \mu_{eff} \frac{\partial k}{\partial x_i} \right) + \mu_{eff} S^2 - \rho \epsilon \quad (8)$$

$$\begin{aligned} \frac{\partial}{\partial t}(\rho \epsilon) + \frac{\partial}{\partial x_i}(\rho u_i \epsilon) &= \frac{\partial}{\partial x_i} \left(\alpha_\epsilon \mu_{eff} \frac{\partial \epsilon}{\partial x_i} \right) + C_{1\epsilon} \frac{\epsilon}{k} \mu_{eff} S^2 \\ &- C_{2\epsilon} \rho \frac{\epsilon^2}{k} - R \end{aligned} \quad (9)$$

where α_k and α_ϵ are the inverse of the effective Prandtl numbers for k and ϵ , respectively, and are computed using an expression derived analytically from the RNG theory.

$$\left| \frac{\alpha - 1.3929}{\alpha_0 - 1.3929} \right|^{0.6321} \left| \frac{\alpha + 2.3929}{\alpha_0 + 2.3929} \right|^{0.3679} = \frac{\mu}{\mu_{eff}} \quad (10)$$

where $\alpha_0 = 1.0$ and $\alpha = \alpha_k = \alpha_\epsilon = 1.393$ at high Reynolds numbers. S is the modulus of the mean rate-of-strain tensor, S_{ij} , which is defined as

$$S \equiv \sqrt{2S_{ij}S_{ij}} \quad (11)$$

and R is

$$R = \frac{C_\mu \rho \gamma^3 (1 - \frac{\gamma}{\gamma_0}) \epsilon^2}{1 + \beta \gamma^3} \frac{k}{k} \quad (12)$$

where $\gamma = Sk/\epsilon$, $\gamma_0 = 4.38$, and $\beta = 0.012$. The constants for this model are listed in Table 3.

Table 3: Constants for the RNG Turbulence Model

C_μ	0.0845
$C_{1\epsilon}$	1.42
$C_{2\epsilon}$	1.68

4.3.3 RSM Model

The Reynolds Stress Model (RSM) differs significantly from the standard and RNG $k-\epsilon$ turbulence models in that it has separate transport equations for each of the Reynolds stresses, thus allowing for anisotropy in the turbulent diffusivity as well as accounting for "history effects" on the individual Reynolds stresses. This model does not fall into the framework set-up by the Boussinesq hypothesis. The transport equations for the individual Reynolds stresses are:

$$\begin{aligned} \frac{\partial}{\partial t}(\overline{u_i' u_j'}) + u_k \frac{\partial}{\partial x_k}(\overline{u_i' u_j'}) &= \\ - \frac{\partial}{\partial x_k} \left[(\overline{u_i' u_j' u_k'}) + \frac{p'}{\rho} (\delta_{kj} u_i' + \delta_{ik} u_j') - \nu \frac{\partial}{\partial x_k}(\overline{u_i' u_j'}) \right] \\ - \left[\overline{u_i' u_k'} \frac{\partial u_j}{\partial x_k} + \overline{u_j' u_k'} \frac{\partial u_i}{\partial x_k} \right] \\ + \frac{p'}{\rho} \left[\frac{\partial u_i'}{\partial x_j} + \frac{\partial u_j'}{\partial x_i} \right] - 2\nu \left[\frac{\partial u_i'}{\partial x_k} \frac{\partial u_j'}{\partial x_k} \right] \\ - 2\Omega_k [\overline{u_j' u_m'} \epsilon_{ikm} + \overline{u_i' u_m'} \epsilon_{jkm}] \end{aligned} \quad (13)$$

The diffusive transport, the first term on the right hand side of Equation 13, is modeled using a scalar diffusion coefficient and the high Reynolds number assumption, $v_T \gg v$. (Shir, 1973):

$$Diffusive\ Transport = \frac{\partial}{\partial x_k} \left(\frac{\nu_t}{\sigma_k} \frac{\partial(\overline{u_i' u_j'})}{\partial x_k} \right) \quad (14)$$

The pressure strain term in Equation 13 is modeled as (Lauder, 1989; Lauder et al., 1975):

$$\begin{aligned} \frac{p'}{\rho} \left[\frac{\partial u_i'}{\partial x_j} + \frac{\partial u_j'}{\partial x_i} \right] &= - C_1 \frac{\epsilon}{k} \left[\overline{u_i' u_j'} - \frac{2}{3} \delta_{ij} k \right] \\ - C_2 \left[P_{ij} - \frac{2}{3} \delta_{ij} P - S_{ij} \right] \end{aligned} \quad (15)$$

where C_1 and C_2 are empirical constants, $P = 1/2 P_{ij}$, and

$$P_{ij} = - \overline{u_i' u_k'} \frac{\partial u_j}{\partial x_k} - \overline{u_j' u_k'} \frac{\partial u_i}{\partial x_k} \quad (16)$$

The dissipation term is considered to be isotropic and is modeled as (Rodi, 1984):

$$2\nu \frac{\partial u_i'}{\partial x_k} \frac{\partial u_j'}{\partial x_k} = \frac{2}{3} \delta_{ij} \epsilon \quad (17)$$

The turbulence dissipation rate, ε , is calculated using Equation 4. The constants for the RSM model are listed in Table 4.

Table 4: Constants for the RSM Turbulence Model

C_μ	0.09
$C_{1\varepsilon}$	1.44
$C_{2\varepsilon}$	1.92
C_1	1.8
C_2	0.6
σ_ε	1.3
σ_k	1.0

4.5 Near Wall Treatments

Three different near wall treatments were used in combination with the aforementioned turbulence models: generalized wall functions, non-equilibrium wall functions, and the two-layer zonal model.

4.4.1 Generalized Wall Functions

The generalized wall functions (Launder and Spalding, 1974) are applied in Fluent/UNS when $y^* > 11.225$, where

$$y^* \equiv \frac{\rho C_\mu^{1/4} k_p^{1/2} y_p}{\mu} \quad (18)$$

The law-of-the-wall for mean velocity yields

$$U^* = \frac{1}{K} \ln(Ey^*) \quad (19)$$

where

$$U^* \equiv \frac{U_p C_\mu^{1/4} k_p^{1/2}}{\tau_w / \rho} \quad (20)$$

The law of the wall for temperature is

$$T^* = \begin{cases} Pr y^* & (y^* < y_T^*) \\ Pr_i \left[\frac{1}{K} \ln(Ey^*) + P \right] & (y^* > y_T^*) \end{cases} \quad (21)$$

where y_T^* is the non-dimensional thermal sublayer thickness computed as the y^* value at which the linear law and logarithmic law in equation 21 intersect and

$$T^* \equiv \frac{(T_w - T_p) \rho C_p C_\mu^{1/4} k_p^{1/2}}{q''} \quad (22)$$

and

$$P = \frac{\pi/4}{\sin(\pi/4)} \left(\frac{A}{K} \right)^{1/2} \left(\frac{Pr_i}{Pr} - 1 \right) \left(\frac{Pr_i}{Pr} \right)^{1/4} \quad (23)$$

The boundary condition for k at the wall is given by

$$\frac{\partial k}{\partial n} = 0 \quad (24)$$

where n is the local coordinate normal to the wall. Therefore, generation of k is calculated using

$$G_k \approx \tau_w \frac{\partial U}{\partial y} = \tau_w \frac{\tau_w}{\kappa \rho C_\mu^{1/4} k_p^{1/2} y_p} \quad (25)$$

and ε is computed from

$$\varepsilon_p = \frac{C_\mu^{3/4} k_p^{3/2}}{\kappa y_p} \quad (26)$$

4.4.2 Non-equilibrium Wall Functions

In contrast to the generalized wall functions, the non-equilibrium wall functions are made more sensitive to pressure gradients and streamline curvature effects and allow for the imbalance of turbulent production and dissipation. The log-law for mean velocity is then changed to

$$\frac{\bar{U} C_\mu^{1/4} k_p^{1/2}}{\tau_w / \rho} = \frac{1}{K} \ln \left(E \frac{\rho C_\mu^{1/4} k_p^{1/2} y}{\mu} \right) \quad (27)$$

where

$$\bar{U} = U - \frac{1}{2} \frac{dp}{dx} \left[\frac{y_v}{\rho \kappa^{*} k^{1/2}} \ln \left(\frac{y}{y_v} \right) + \frac{y - y_v}{\rho \kappa^{*} k^{1/2}} + \frac{y_v^2}{\mu} \right] \quad (28)$$

and y_v is the physical viscous sublayer thickness defined as

$$y_v \equiv \frac{\mu y^*}{\rho C_\mu^{1/4} k_p^{1/2}} \quad (29)$$

where $y_v^* = 11.225$. In order to allow for the imbalance of turbulent production and dissipation at the wall, the following assumptions are made:

$$\tau_i = \begin{cases} 0, & y < y_v \\ \tau_w, & y > y_v \end{cases} \quad (30)$$

$$k = \begin{cases} \left(\frac{y}{y_v} \right)^2 k_p, & y < y_v \\ k_p, & y > y_v \end{cases} \quad (31)$$

$$\varepsilon = \begin{cases} \frac{2 \nu k}{y^2}, & y < y_v \\ \frac{k^{3/2}}{C_1 y}, & y > y_v \end{cases} \quad (32)$$

where $C_1 = \kappa C_\mu^{-3/4}$. The cell-averaged production of k and its cell averaged dissipation rate can be computed from the volume-average of G_k and ε of the wall-adjacent cells.

$$\bar{G}_k \equiv \frac{1}{2y_p} \int_0^{2y_p} \tau_i \frac{\partial U}{\partial y} dy \quad (33)$$

$$\bar{\varepsilon} \equiv \frac{1}{2y_p} \int_0^{2y_p} \varepsilon dy \quad (34)$$

This volume-average changes for different grid topologies.

4.4.3 Two-layer Zonal Model

The two-layer zonal model for near wall treatment documented in Fluent/UNS (1996) eliminates the use of wall functions and divides the flow field into a viscosity-affected region and a fully turbulent region. The two regions are defined using the turbulent Reynolds number, Re_y , where

$$Re_y \equiv \frac{\rho \sqrt{k} y}{\mu} \quad (35)$$

In the fully turbulent region, $Re_y > 200$, the standard $k-\varepsilon$ turbulence model is employed. For the near wall viscosity-affected region, $Re_y < 200$, the one equation model of Wolfstein (1969) is used. In this model,

the momentum and k equations from the standard $k-\epsilon$ model as described above are retained, but μ_t is calculated with

$$\mu_t = \rho C_\mu \sqrt{k} l_\mu \quad (36)$$

The turbulent dissipation field is calculated using

$$\epsilon = \frac{k^{3/2}}{l_\epsilon} \quad (37)$$

The length scales in Equations 36 and 37 are computed by

$$l_\mu = C_D \left[1 - \exp\left(-\frac{Re_y}{A_\mu}\right) \right] \quad (38)$$

$$l_\epsilon = C_D \left[1 - \exp\left(-\frac{Re_y}{A_\epsilon}\right) \right] \quad (39)$$

where $C_D = \kappa C_\mu^{-3/4}$, $A_\mu = 70$, and $A_\epsilon = 2C_D$ (Chen and Patel, 1988).

5. RESULTS AND DISCUSSION

Although the methodology employed in the present study isolates the true performance of the turbulence treatments under investigation, some criteria are necessary to determine how satisfactory the results are from these treatments. Therefore, the results from each simulation will be compared to the results of the other simulations and code validation quality experimental data in order to determine which turbulence treatment is most effective. An understanding of the physics of the flowfield and the surface results will facilitate this evaluation. A secondary issue involving computational intensity and resources needed to employ these turbulence treatments will be documented at the end of this section.

5.1 Flowfield Results

Although a strong interdependence of the flow in the plenum, film hole, and crossflow exists, each critical region of the flowfield is examined separately to highlight the influence that region has on the surface results. The REF1 case will be used in this analysis because it has a realistic density ratio, $DR=2$. This section focuses primarily on the effects of the turbulence treatments on the predicted field and surface results.

5.1.1 Film Hole and Plenum

As documented in Leyle and Zerkle (1994) and Walters and Leyle (1997a), separation and flow turning near the film-hole entrance result in a "jetting" region along the upstream wall as well as counter-rotating secondary flow within the film hole. Turbulence should be produced in the shear layers created at the interface of this jetting region and the low momentum pocket on the downstream wall of the film hole. Figure 2 shows the turbulence level in the film hole centerplane of the REF1 cases. Pietrzyk et al. (1989) measured turbulence levels on the order of 10% exiting a film hole of $L/D=3.5$, $M=0.5$, $DR=2$. Since the REF1 case has a $L/D=1.75$, the turbulence level should be even higher because the short film hole does not give the turbulence an opportunity to attenuate. All the standard $k-\epsilon$ models with any of the wall treatments show this relatively high level of turbulence. Figure 2 (a,b,g). However, the turbulence levels are significantly lower in the cases with the RNG and RSM models, Figure 2 (c-f). Since the production of turbulence within the film hole is dominated by what happens away from the walls, differences in results between the generalized wall functions and non-equilibrium wall functions in each case are exceptionally small. In fact, the differences between the generalized wall functions and the non-equilibrium wall functions were found to be small

in all the cases studied; therefore, unless otherwise mentioned, the cases involving non-equilibrium wall functions will not be documented in the rest of the paper.

The REF1-KE-2L case shows significantly higher turbulence levels than any of the other cases in Figure 2g. This behavior can be traced back to the turbulence treatment. The two-layer zonal model algebraically prescribes a length scale within regions with $Re_y < 200$. Because the velocity in the plenum region is so low, this algebraically prescribed length scale is applied to most of the plenum. Therefore, the length scale, a function of distance from the wall, is too large, making the turbulent dissipation rate, ϵ , too low. The low value of ϵ causes a higher level of turbulence production as the flow is rapidly strained while entering the film hole. The algebraic prescription of the length scale is appropriate for boundary layer flows; however, in the plenum, which acts much like a pressurized vessel with creeping flow, this treatment fails to supply an appropriate length scale and results in higher turbulence levels within the film hole and downstream of the film hole exit. The wall functions are better able to handle turbulence quantities in the plenum.

5.1.2 Near Field of Jet-Crossflow Interaction

Extremely complex flow features are formed as the coolant jet interacts with the crossflow. As shown in Walters and Leyle (1997b), the dominant flow feature is not turbulence related; instead, the counter-rotating vortices formed at the edge of the film-hole exit dominate the flowfield. Figure 3 shows contours of streamwise vorticity at $x/D=1$ for the different turbulence treatments.

For each case, the counter-rotating vortices in the crossflow are formed due to the vorticity contained in the boundary layer of the film hole. Thus, for cases using wall functions to resolve much of the boundary layer flow, the vortex structures are nearly identical. Each show the maximum vorticity to be within the first layer of cells. Thus, the two-layer zonal model, which does not use the wall functions but actually resolves the sublayer, shows a slightly different vorticity pattern with a higher magnitude. Although the flow characteristics in each case are very similar, the turbulence level of the coolant exiting from the film hole is extremely varied. The higher turbulence levels in the film hole shown in Figure 2 are carried out of the film hole and downstream by the coolant jet. However, in the near field region, the effects of the different turbulence levels from case to case for REF1 is minimal when compared to the effects of the counter-rotating vortices.

The major difference between the turbulence treatments in the near field region is a result of the near wall treatments. As documented in Walters and Leyle (1997b), the two-layer zonal model resolves the small separation region at the trailing edge of the film hole. This separation region is formed when the jet lifts off the test surface and allows the crossflow to tuck under the jet. Figure 4 shows the saddle point and reverse flow just downstream of the trailing edge of the film hole. This flow mechanism will have serious effects on the surface results but is missed by both the generalized and non-equilibrium wall functions when used in conjunction with any of the turbulence models.

5.1.3 Far Field of Jet and Crossflow Interaction

As the jet and crossflow move downstream, the counter-rotating vortices dissipate and the turbulent diffusion plays a greater role in the spreading of the jet. Figure 5 shows contours of turbulence levels at several x/D

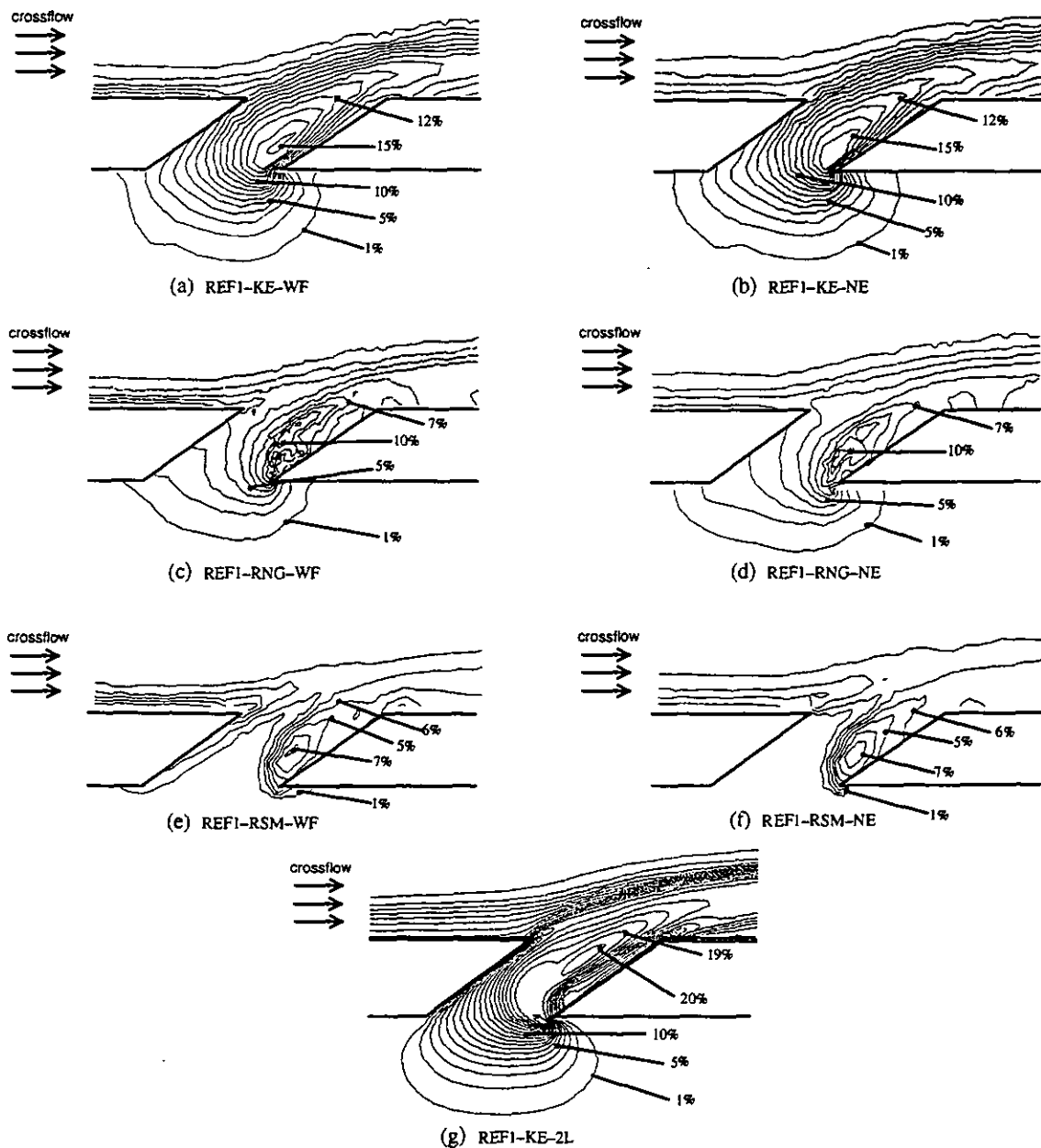


Figure 2. Turbulence level at the film hole centerline for (a) REF1-KE-WF, (b) REF1-KE-NE, (c) REF1-RNG-WF, (d) REF1-RNG-NE, (e) REF1-RSM-WF, (f) REF1-RSM-NE, and (g) REF1-KE-2L for $M=1$, $DR=2$, and $L/D=1.75$.

stations downstream of the film hole. As the turbulence generated within the film hole is convected downstream, the higher turbulence levels of the $k-\epsilon$ models show more dissipation of the coolant jet consistent with the excessive turbulence in the film hole. Figure 6 shows the temperature contours at the same x/D locations for each of the cases. As expected, the cases with the higher turbulence levels show more diffusion of the coolant jet. The RSM and RNG cases show little thermal diffusion, and the core of the jet remains relatively uninfluenced by the crossflow. This behavior is also consistent with the low turbulence levels found within the film hole and convected downstream.

5.2 Surface Results

5.2.1 Adiabatic Effectiveness

The REF1 case was used in conjunction with experimental data from Sinha et al. (1990) to analyze the performance of turbulence models in calculating the adiabatic effectiveness. Figure 7 shows centerline and lateral variations of η for experimental and computational results.

As Figures 7 (a,c) show, every turbulence model performed well for $x/D > 10$. In addition, every case using wall functions showed similar results. Nevertheless, the surface results, while similar, do show behavior

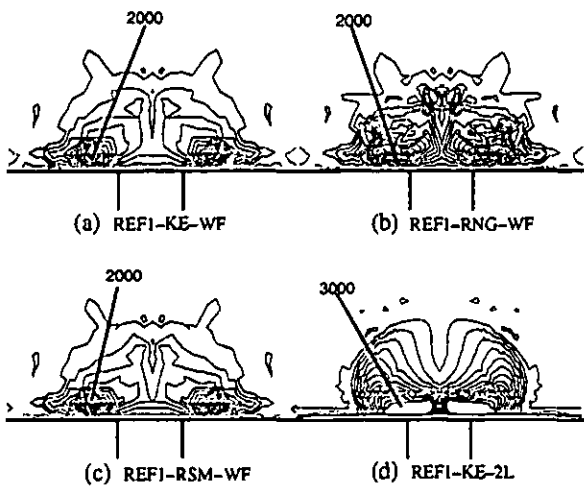


Figure 3. Contours of streamwise vorticity at $x/D=1$ show the vorticity magnitude is the same in the (a) REF1-KE-WF, (b) REF1-RNG-WF, (c) REF1-RSM-WF, and (d) REF1-KE-2L cases for $L/D=1.75$, $M=1$, $DR=2$.

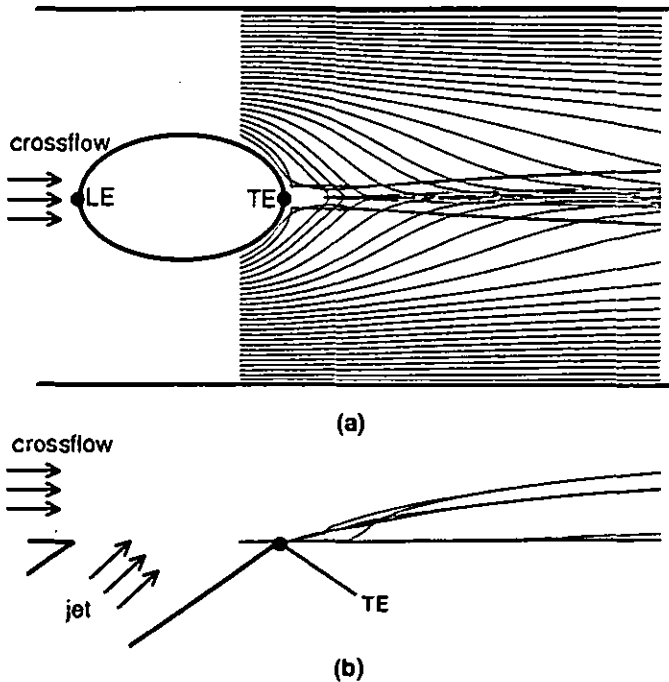


Figure 4. Particle pathlines show saddle point and reverse flow downstream of the trailing edge for the REF1-KE-2L case—(a) top view, (b) side view.

consistent with the flowfield results. For all of the RNG $k-\epsilon$ and RSM cases, the low turbulence levels decreased the diffusion of the coolant, thus increasing η along the centerline. The REF1-KE-WF and REF1-KE-NE cases show higher turbulence levels which result in enhanced diffusion of the coolant and decreased η along the centerline.

The most significant difference among the turbulence models is shown in the near field region where the REF1-KE-2L greatly outperforms the other turbulence treatments by more accurately matching the experimental data over the entire test surface. Because the two-layer zonal model captures the separation region at the trailing edge of the film hole, the hot crossflow tucks in under the coolant jet and markedly decreases the centerline η . Fig. 7(a,b) shows the decreased η for the REF1-KE-2L case. Much of the remaining discrepancy between the REF1-KE-2L case and the results of Sinha et al. (1990) can be attributed to the experimental jet skewness documented in Walters and Leylek (1997a). Given the fact that the ability of CFD simulations to capture coolant lift-off is highly desirable, the failure of wall functions to capture this drastic change in η dramatically reveals their limitations in design situations.

5.2.2 Heat Transfer Coefficient

The REF2 case and experimental data from Sen (1995) were used to analyze the ability of the turbulence models to calculate the heat transfer coefficient. Figure 8 (a–c) show the normalized heat transfer coefficient for both variations along the centerline and lateral variations. Because the non-equilibrium wall functions did not produce significant changes in either the flowfield or the adiabatic effectiveness results, cases with these wall functions were not computed. For each of the turbulence treatments, two simulations were run: one to calculate the heat transfer coefficient with film cooling, h_f , and another to compute the heat transfer coefficient without film cooling, h_0 . The ratio, h_f/h_0 , is plotted in Figure 8.

Figure 8 shows reasonably good agreement between computational and experimental results. The REF2-RSM-WF case proved to be most consistent with experimental results downstream of the trailing edge. However, it completely fails to capture the augmentation of h_f/h_0 near the trailing edge. Nevertheless, both the REF2-KE-WF and REF2-RNG-WF cases give consistent results for h_f/h_0 , especially near of the trailing edge, where $x/D < 3$.

5.3 Computational Intensity

Just as the performance of each turbulence treatment may differ significantly, the computational intensity of and the resources required for each treatment also may vary. Using the REF1-KE-WF case as the reference point, this section will give estimates of the significant differences in computational intensity among the different turbulence treatments. These estimates are based on data compiled while running simulations for each turbulence treatment.

The RNG turbulence model adds little to the computational intensity of the simulation relative to the $k-\epsilon$ model. However, the RSM model adds six new transport equations to the simulation, increasing the required memory resources by 20% and increasing the cpu time per iteration by 65%. In addition, the new transport equations cause the simulation to have an extremely low convergence rate. The RSM model requires at least 30% more iterations to reach convergence.

Among the near-wall treatments, the different wall functions produce negligible differences in the computational intensity. However, the two-layer zonal model requires significantly more resources. In addition to needing nearly 50% more finite volumes in the computational mesh, the two-layer zonal model creates an extremely stiff set of equations that requires nearly 30% more iterations to bring to convergence. The memory usage increases by almost 20%, and the cpu time per iteration increases by nearly 60%. Although the two-layer zonal model produces a remarkable increase in the accuracy of the computational simulations, the huge resources required to use it effectively highlight the fact that the more eco-

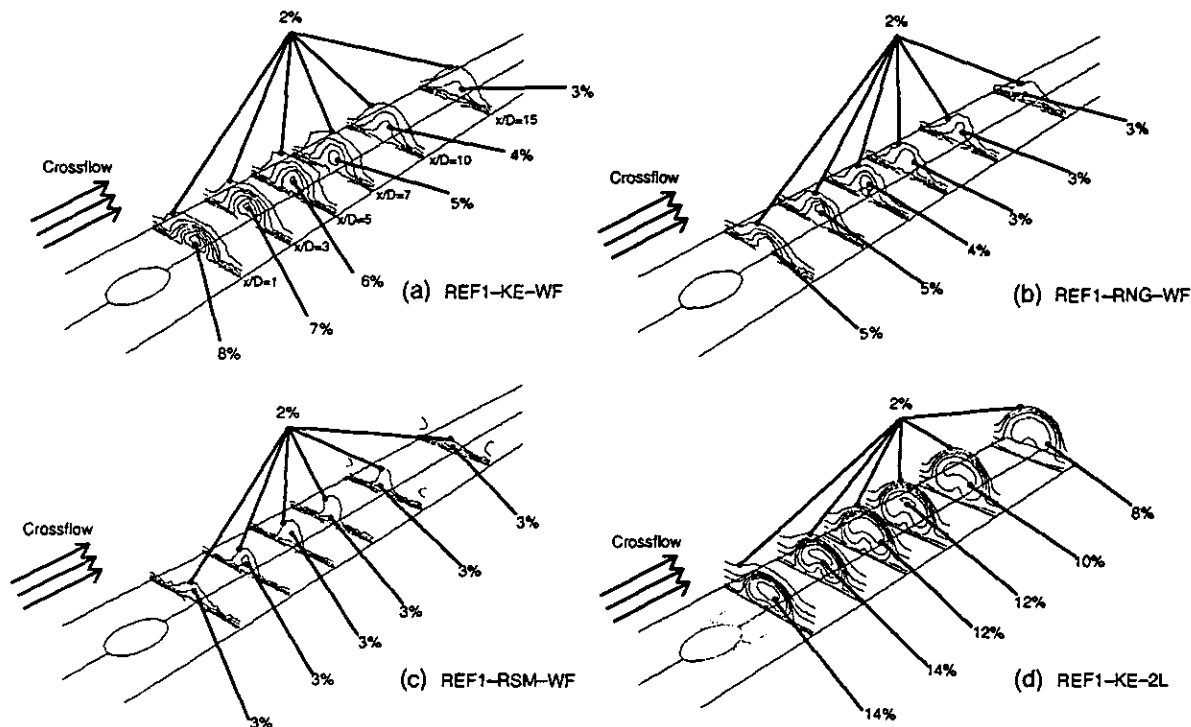


Figure 5. Contours of turbulence level at $x/D=1, 3, 5, 7, 10$, and 15 downstream of the film hole for (a) REF1-KE-WF, (b) REF1-RNG-WF, (c) REF1-RSM-WF, and (d) REF1-KE-2L cases for $L/D=1.75$, $M=1$, $DR=2$.

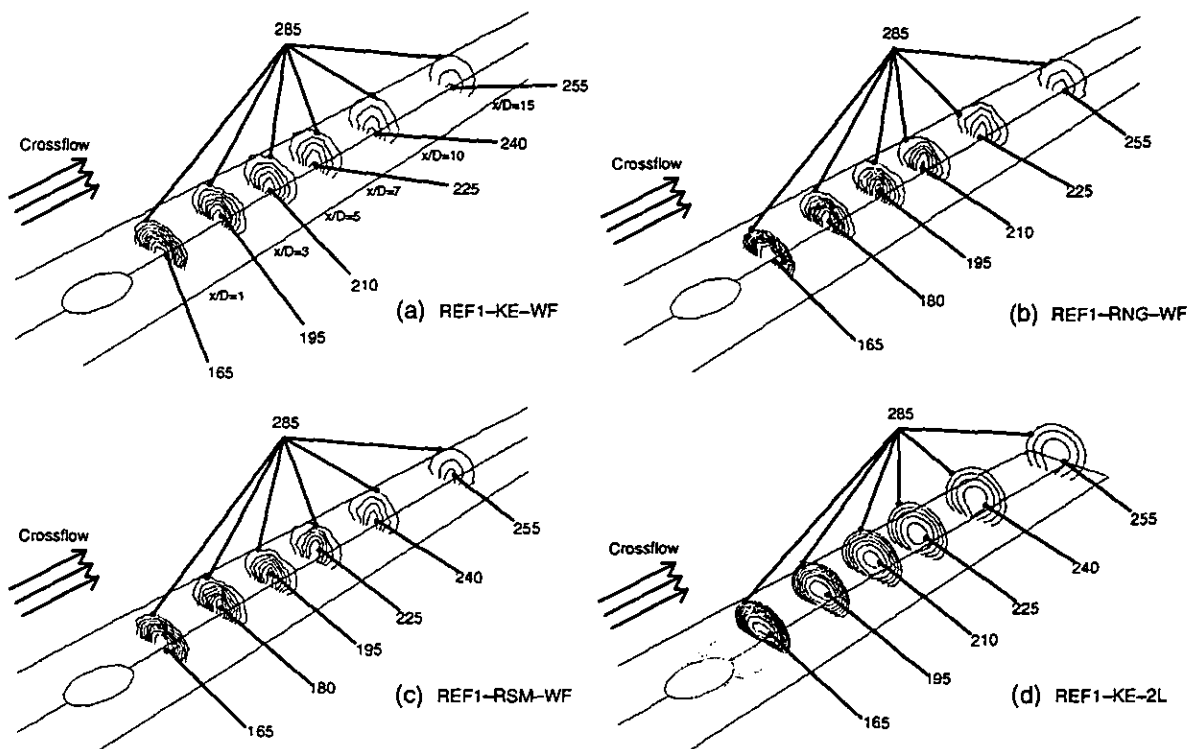
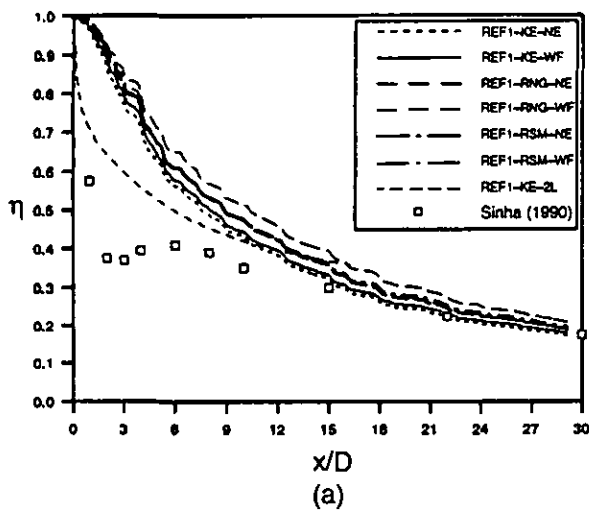
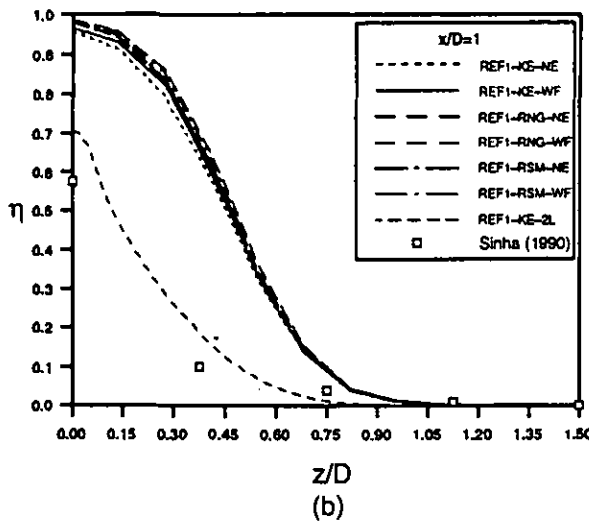


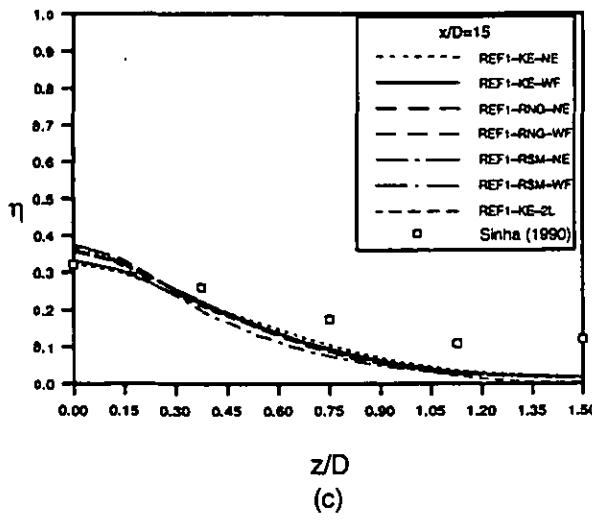
Figure 6. Temperature [K] contours at $x/D=1, 3, 5, 7, 10$, and 15 downstream of the film hole for (a) REF1-KE-WF, (b) REF1-RNG-WF, (c) REF1-RSM-WF, and (d) REF1-KE-2L cases for $L/D=1.75$, $M=1$, $DR=2$.



(a)

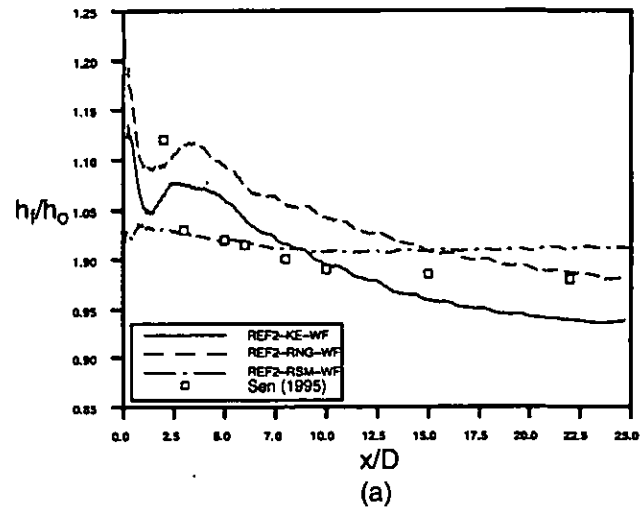


(b)

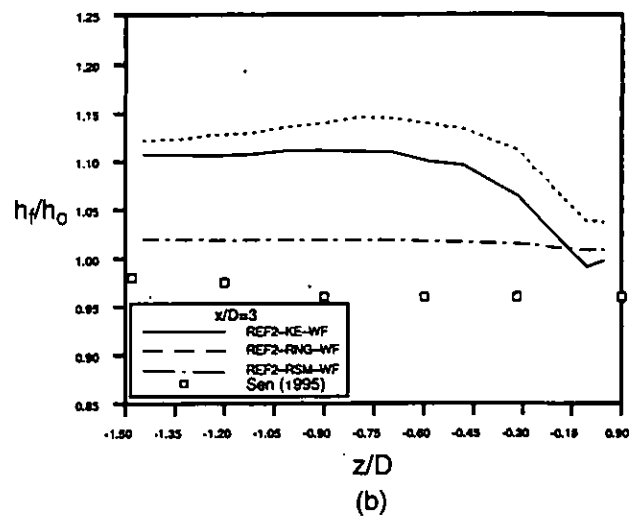


(c)

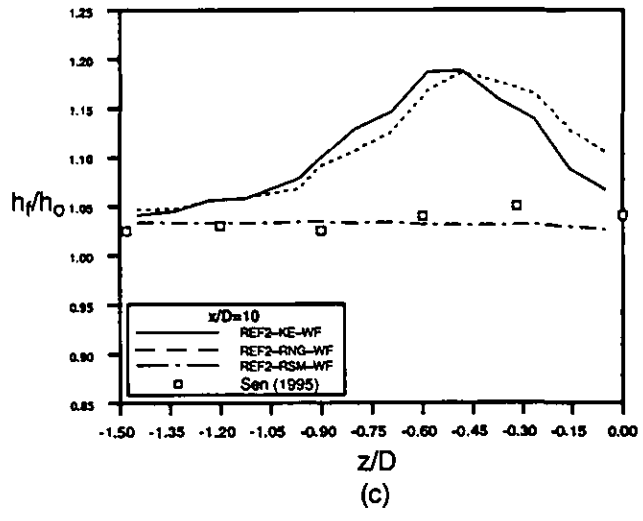
Figure 7. Adiabatic effectiveness data for $L/D=1.75$, $M=1$, $DR=2$: (a) variations along the centerline; (b) lateral variations at $x/D=1$; and (c) lateral variations at $x/D=15$.



(a)



(b)



(c)

Figure 8. Normalized heat transfer coefficient for $L/D=4$, $M=1$, $DR=1$: (a) variations along centerline; (b) lateral variations at $x/D=3$; and (c) lateral variations at $x/D=10$

nomical wall functions can still provide great insight into flow problems and may be more desirable in a design environment where fast turn-around time is critical.

6. CONCLUSIONS

The present study used a well-tested, highly reliable computational methodology in conjunction with code validation quality experimental data to isolate the true performance of seven turbulence treatments. The key conclusions drawn in this study are as follows:

- Of the three turbulence models examined, the standard k- ϵ model performed better than the RNG and RSM models in their present form. Specifically, the turbulence level predicted by the standard k- ϵ model was more in-line with experimental measurements.
- Of the three near-wall treatments analyzed in the present study, the two-layer zonal model produced solutions more consistent with experiments than the generalized or non-equilibrium wall functions. The small separation bubble associated with the coolant jet lift-off and reattachment could only be captured through the viscous sublayer resolution made possible by the two-layer approach.
- The RNG model could benefit from some more development effort. Low thermal diffusion of the coolant jet resulting from unusually low levels of turbulence augmentation relative to experimental measurements requires special attention. The RNG model has the potential to be competitive given its relative simplicity and economic feasibility in computational simulations.
- By far the most complex and sophisticated model requiring substantially higher computational intensity is the RSM model. It needs to perform significantly better than the other models tested in the present study before its use can be justified in a design environment.
- Convergence rate decreases and overall cpu time rises sufficiently in simulations employing the two-layer near-wall treatment to warrant a serious cost-benefit analysis over the wall function approach.
- For the class of problems studied, the wall function approach can provide results to assess the relative performance of different film cooling configurations; however, many small scale flow features will be masked by the wall functions. More details of the flow can be resolved with the use of a two-layer zonal model.
- The two-layer near-wall treatment is not well suited to the low Re_y values found in the plenum region. The unrealistically high length scales applied to the low velocity fluid in the plenum result in a low value of ϵ and a higher level of turbulence production as the flow is rapidly strained while entering the film hole.
- The ability to knowledgeably and realistically apply different turbulence models and near-wall treatments to different regions of the computational domain could greatly increase the consistency between computations and experiments.

REFERENCES

- Chen, H. and Patel, V., 1988, "Near-Wall Turbulence Models for Complex Flows Including Separation," *AIAA Journal*, Vol. 26, No. 6, pp. 641-648.
Demuren, A., 1982, "Numerical Calculation of Steady Three-Dimensional Turbulent Jets in Cross Flow," Rep. SFB 80/T/129. Sonderforschungsbereich 80, University of Karlsruhe.
Fluent/UNS Users' Guide, May 1996, Release 4.2.5, Fluent Incorporated, Lebanon, NH.

- Garg, V. and Gaugler, R., 1995, "Effect of Velocity and Temperature Distribution at the Hole Exit on Film Cooling of Turbine Blades," ASME Paper No. 95-GT-2.
Garg, V. and Ameri, A., 1997, "Comparison of Two-equation Turbulence Models for Prediction of Heat Transfer on Film-cooled Turbine Blades," Presented at the IGTI Turbo Exposition, Orlando, Florida, ASME Paper No. 97-GT-24.
Hosseinalipour, S. and Mujumdar, A., 1995, "Comparative Evaluation of Different Turbulence Models for Confined Impinging and Opposing Jet Flows," *Numerical Heat Transfer, Part A*, Vol. 28, pp. 647-666.
Lauder, B., Reece, J., and Rodi, W., 1975, "Progress in the Development of a Reynolds-stress Turbulence Closure," *Journal of Fluid Mechanics*, Vol. 68, Part 3, pp. 537-566.
Lauder, B. and Spalding, D., 1972, *Lectures in Mathematical Models of Turbulence*, Academic Press, London, England.
Lauder, B. and Spalding, D., 1974, "The Numerical Computation of Turbulent Flows," *Computer Methods in Applied Mechanics and Engineering*, Vol. 3, pp. 269-289.
Leylek, J. and Zerkle, R., 1994, "Discrete-Jet Film Cooling: A Comparison of Computational Results with Experiments," *Journal of Turbomachinery*, Vol. 116, pp. 358-368.
Pietrzyk, J., Bogard, D., and Crawford, M., 1989, "Experimental Study of the Interaction of Dense Jets with a Crossflow for Gas Turbine Applications," Report No. 89-1, University of Texas at Austin.
Rodi, W., 1984, *Turbulence Models and Their Application in Hydraulics*, IAHR, Delft, The Netherlands.
Sarkar, S. and Bose, T., 1995, "Comparison of Different Turbulence Models for Prediction of Slot-film Cooling: Flow and Temperature Field," *Numerical Heat Transfer, Part B*, Vol. 28, pp. 217-238.
Schmidt, D., Sen, B., and Bogard, D., 1994, "Film Cooling with Compound Angle Holes: Adiabatic Effectiveness," ASME Paper No. 94-GT-312.
Sinha, A., Bogard, D., and Crawford, M., 1990, "Film Cooling Effectiveness Downstream of a Single Row of Holes with Variable Density Ratio," ASME Paper No. 90-GT-43.
Sen, B., 1995, "Effects of Injection Hole Geometry, High Freestream Turbulence, and Surface Roughness on Film Cooling Heat Transfer," Ph.D. Dissertation, University of Texas at Austin.
Sharif, M. and Wong, Y., 1994, "Evaluation of the Performance of Three Turbulence Closure Models in the Prediction of Confined Swirling Flows," Pergamon, 0045-7930(94)E0004-H.
Shir, C., 1973, "A Preliminary Study of Atmospheric Turbulent Flow in the Idealized Planetary Boundary Layer," *Journal of Atmospheric Science*, Vol. 30, pp. 1327.
Walters, D. and Leylek, J., 1997a, "A Systematic Computational Methodology Applied to a Three-Dimensional Film-Cooling Flowfield," *Journal of Turbomachinery*, Vol. 119, pp. 777-785.
Walters, D. and Leylek, J., 1997b, "A Detailed Analysis of Film-Cooling Physics Part I: Streamwise Injection with Cylindrical Holes," Presented at the IGTI Turbo Exposition, Orlando, Florida, ASME Paper No. 97-GT-269.
Wolfstein, M., 1969, "The Velocity and Temperature Distribution of One-Dimensional Flow with Turbulence Augmentation and Pressure Gradient," *International Journal of Heat and Mass Transfer*, Vol. 12, pp. 301-318.
Yakhot, V. and Orszag, S., 1986, "Renormalization Group Analysis of Turbulence: I. Basic Theory," *Journal of Scientific Computing*, Vol. 1, No. 1, pp. 1-51.